

Central European Journal of Energetic Materials

ISSN 1733-7178; e-ISSN 2353-1843

Copyright © 2025 Łukasiewicz Research Network - Institute of Industrial Organic Chemistry, Poland

Cent. Eur. J. Energ. Mater. 2025, 22(3): 302-343; DOI 10.22211/cejem/211368

Supporting Information is available in PDF-format, in colour, at: https://ipo.lukasiewicz.gov.pl/wydawnictwa/cejem-woluminy/vol-22-nr-3/



Article is available under the Creative Commons Attribution-Noncommercial-NoDerivs BY NC ND 3.0 license CC BY-NC-ND 3.0.

Research paper

Performance of Copper Complex (Cu-en) Combustion Catalyst in the Al/CuO System and Optimization of Electrostatic Spraying Process through **ANSYS Simulation**

Wei Ji*), Yilong Duan, Lei Liu, Lingxin Wang

College of National Defense Science and Technology, Southwest University of Science and Technology, Mianyang, 621010, China * *E-mail*: 17745441207@163.com

Abstract: The Al/CuO system represents a classic thermite reaction system. However, due to limitations such as the relatively low solid-phase reaction rate between the aluminium oxide (Al₂O₃) film and the Al/CuO system, it has gradually been replaced by other systems. To address these limitations, this study introduces a copper complex (Cu-en) combustion catalyst into the Al/CuO system, leveraging its thermal decomposition characteristics and high catalytic activity. Three distinct preparation methods-electrostatic spraying, spray drying, and solvent evaporationwere employed to synthesize composite materials. Differential Scanning Calorimetry (DSC) analysis demonstrated that the electrostatic spraying method yielded the most favorable performance, with an exothermic peak advancing to 353.13 °C and a heat release of 4702.05 J/g. For the spray drying method, two exothermic peaks were observed at 383.04 and 782.94 °C, with a total heat release of 2309.16 J/g. In contrast, the original Al/CuO system and the composite prepared via solvent evaporation did not exhibit any thermite reaction exothermic peaks. Combustion tests revealed that the composite prepared using the electrostatic spraying method exhibited an exceptionally high combustion rate, the widest range of burning speeds, and a response time within 0.5 ms. This phenomenon was further confirmed by SEM (Scanning Electron Microscopy) analysis, which showed that the composites prepared via electrostatic spraying had the highest degree of sphericity, the smallest particle size, and a uniform distribution of Al and CuO on the spherical surface. A series of tests indicated that introducing Cu-en into the Al/CuO system, combined with the electrostatic spraying method, effectively improved the issues of instability and slow reaction rates in the Al/CuO thermite system. Furthermore, this study utilized ANSYS finite element software to simulate the effects of flow rate, voltage, and receiving distance on particle size during the electrostatic spraying process. An orthogonal experimental design was employed to optimize the electrostatic spraying process, ensuring that the preparation of composites via electrostatic spraying achieved the best possible results.

Keywords: thermite reaction, Al/CuO, combustion catalysts, electrostatic spraying, ANSYS simulations

Abbreviations:

- f Air resistance, also known as Stokes drag
- r Droplet radius
- v Droplet velocity
- $F_{\rm s}$ Surface tension
- F_a Electric field force
- E Electric field intensity
- F_r Electrostatic repulsion force between droplets
- G Gravity
- Δl The change in the droplet surface area
- η Air viscosity
- q The charge carried by the droplet
- σ Surface tension coefficient
- μ Viscosity
- φ Electric potential
- ρ_e Charge density
- ε Dielectric constant

1 Introduction

Thermites are energetic materials composed of aluminium powder as the reducing agent and metal oxides as the oxidizing agent. The combustion reactions of thermites release substantial amounts of heat and generate temperatures of extreme magnitude, which has led to their extensive utilisation in industrial, military, and civil applications. Conventional thermites are typically composed of aluminium powder and iron oxide, with reaction products including molten iron and aluminium oxide (Al₂O₃). These thermites exhibit high energy release, with reaction enthalpies up to 850 kJ/mol [1-3]. Among these, the Al/CuO system is widely regarded as the most classical of the thermite reactions. This is due to

the fact that it is a relatively simple reaction, capable of producing a superior theoretical heat release, and it exhibits superior thermodynamic properties. The reason for this can be ascribed to the low reduction potential of aluminium (-1.66 V) and the high oxidation potential of copper oxide (+0.34 V). When these two elements are combined, they create a high degree of electrochemical match. Consequently, the Gibbs free energy for the Al/CuO reaction is significantly negative, indicating a high level of spontaneity [4-7]. However, with advancing technology and the ever-evolving demands of modern defense industries, the limitations of the Al/CuO system have become increasingly evident. For instance, the dense Al₂O₃ film that naturally forms on the aluminium surface significantly inhibits its reactivity, preventing spontaneous reactions at low temperatures and necessitating additional ignition energy. Furthermore, the reaction between aluminium and copper oxide primarily depends on solid-phase diffusion, which is relatively slow. This leads to a low solid-phase reaction rate and impedes the full utilization of the system's high energy density [8-10]. To address the aforementioned challenges, researchers have explored the composition, preparation processes, and performance optimisation of thermites in great depth, presenting numerous innovative solutions. These include multicomponent thermites (which introduce other metal oxides or composite oxidizers to enhance reaction product properties), nano-thermites (utilizing nanoscale aluminium powder and oxidizers to significantly improve reaction rates and combustion efficiency), and the addition of combustion catalysts (such as metalorganic compounds or metal oxides) to lower ignition temperatures and enhance combustion uniformity. These endeavours have culminated in numerous research breakthroughs that hold great promise in overcoming the inherent limitations of the Al/CuO system [11].

In relation to the methods of preparation, Yin *et al.* [12] successfully synthesised nano-Al/Fe₂O₃ and nano-Al/CuO using the sol-gel method, while Wang *et al.* [13] prepared n-Al/C-CuO composites by the spray drying process. These approaches have been shown to significantly improve the combustion and thermodynamic properties of aluminium powders. He *et al.* [14] fabricated high-energy-release Al/CuO energetic materials with high energy release by electrophoretic deposition of nano-Al and CuO microboxes on Ti substrates. Under a stoichiometric ratio of 3.0, the Al/CuO energetic material released a maximum heat of 3049 J/g. Lv *et al.* [15] investigated the ignition and combustion performance of *n*-Al/CuO/kerosene nanofluid fuel. Their results demonstrated two exothermic peaks on the DSC curve of *n*-Al/CuO (5%) at 249.3 and 463.8 °C. During the agglomerate combustion phase, *n*-Al/CuO (5%)/kerosene exhibited the shortest ignition delay and the highest emission spectral intensity at 0.057 s.

Furthermore, in terms of additives, Luo et al. [16] summarized the performance enhancement of Al/CuO-based thermites by introducing titanium-containing polymers, silicon-containing polymers, fluorine-containing polymers, and other additives. In addition, Song et al. [17] utilized the spray-drying method to incorporate Cu-en with explosives such as AP, RDX, CL-20, and ε-CL-20, which significantly reduced the exothermic peak temperatures of AP, RDX, β -HMX, and ε -CL-20 to 305.41, 228.61, 280.21, and 232 °C, respectively. The addition of Cu-en, a metal-organic complex, has drastically increased the decomposition temperatures of these energetic materials, demonstrating excellent catalytic performance. Cu-en acts as a combustion catalyst that overcomes the incomplete combustion problems associated with metal oxides. Upon high-temperature decomposition, Cu-en can be transformed in situ into corresponding nonmetal oxides with high catalytic activity, effectively reducing the ignition temperatures and enhancing reaction heat, thus resolving the limitations of Al-based thermites. To achieve uniformly sized Al-based composites with superior performance, this study will employ solvent-antisolvent, solvent-drying, and electrostatic spraying methods to fabricate composites consisting of Al/CuO as the primary reactive system, Cu-en as the combustion catalyst, and F_{2311} as the binder. The prepared composites will be analyzed using DSC, combustion testing, and SEM imaging to evaluate their thermal and combustion properties.

Since electrostatic spraying involves numerous process parameters, improper parameter settings compared to other methods can significantly affect the final experimental results. Therefore, in this study, ANSYS finite element simulation software is utilized to simulate and optimise the process of manufacturing Al-based composites via electrostatic spraying. The specific simulation design adopts a three-factor (voltage, flow rate, and collection distance) and three-level (particle size, velocity, and residence time) orthogonal experimental approach to determine the importance of factors and identify the optimal process conditions. Furthermore, based on the optimised process parameters, a controlled variable experimental method is established to describe the relationships between various levels and factors.

2 ANSYS Finite Element Simulation Analysis

The positive terminal of the power supply is connected to the syringe nozzle, while the negative terminal is attached to the foil collector. A high voltage, typically ranging from several kilovolts to tens of kilovolts, is applied near the nozzle. This high voltage creates a strong electric field between the nozzle and

the target surface. The droplets are attracted to the positive terminal of the power supply due to electrostatic forces, and as a result, adhere accurately to the foil. A schematic of this process is shown in Figure 1.

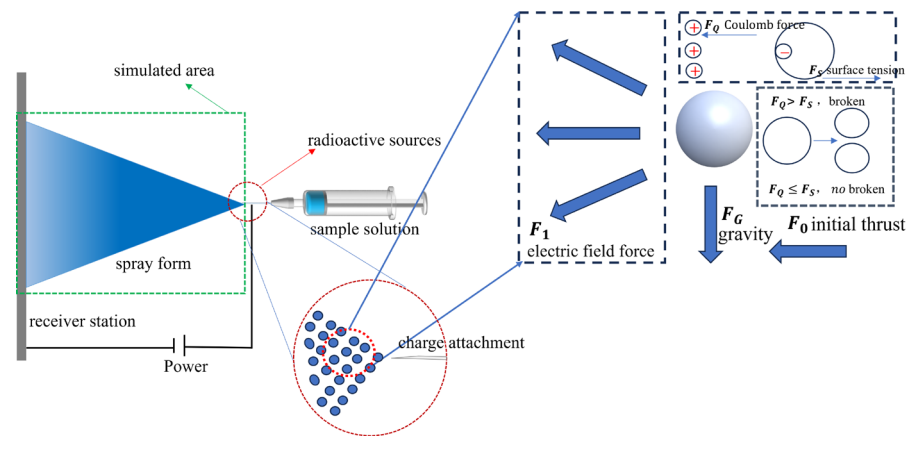


Figure 1. Schematic diagram of electrostatic spray operation

A plethora of researchers have expounded upon the theoretical underpinnings of the droplet breakup in an electric field. For instance, the KH model was employed by Chen et al. [18] to establish the study of droplet fragmentation on COMSOL Multiphysics software, and the scope of application of the KH model and the Taylor model was elucidated. In the context of electrostatic spraying, a liquid droplet subjected to an electrostatic field experiences a multitude of forces, including electric field forces, surface tension, gravity, Coulomb forces, and electrostatic repulsion between the droplets. When the electrostatic force surpasses the surface tension of the liquid, the result is the ejection of very fine charged droplets from the tip of the liquid cone. During the ejection process, the liquid overcomes its own cohesive, resulting in its division into minute particles, thereby creating a uniform atomisation effect. As the charged droplets are subjected to Coulomb forces due to the action of the electric field, they move towards the target surface in the direction of the electric field and are able to cover the complex surfaces of the target object, thus improving the uniformity and efficiency of the spraying. However, not all forces play a dominant role in this process. The model proposed in this study is an idealized model that considers only two dominant forces within the entire electric field: the electric field force and surface tension.

2.1 Electric field establishment and force analysis

In the process of electrostatic spraying, droplets experience a combination of forces under the influence of the electric field, which directly impacts their trajectory, distribution, and final deposition. The electric field force (F_e) arises because the droplets, upon being charged by the emitter, enter the electric field and are subjected to Coulomb force. The F_e is the primary driving force that accelerates the droplets or alters their direction of motion. Its magnitude is proportional to the charge (q) carried by the droplet and the electric field intensity (E) [19]. The expression for the F_e is as follows:

$$F_e = qR \tag{1}$$

Gravity (G) is the force exerted due to the mass of the droplet, acting in the downward direction. In the process of electrostatic spraying, because the droplets are usually very small, the influence of G may be overshadowed by other forces. However, as the droplets move farther from the spraying source, G gradually starts to play a role. This results in the ejected shape typically forming a cone, and farther from the spraying source, G causes some droplets to deviate from the central axis. The expression for G is as follows:

$$G = mg (2)$$

Air resistance (f), also known as Stokes drag, is the resistive force generated by the viscous interaction between the moving droplet and the surrounding air. This force is negligible compared to the effects of surface tension and the F_e . According to Equations 2 and 3, f is related to air viscosity (η) , droplet radius (r), and droplet velocity (v). Since r and η vary minimally, the impact of this force remains relatively constant.

Furthermore, the stronger the F_e , the faster the droplet moves. However, the droplet's velocity in the electric field is inherently limited. If the velocity exceeds a critical value, the droplet may escape the system. Therefore, when performing calculations, f can often be ignored.

$$f = 6\pi \eta r v \tag{3}$$

Surface tension (F_s) is the force that tends to maintain the droplet in a spherical shape, influencing its shape and stability. This force serves as the primary opposition to the F_e during the electrostatic spraying process. According to Equations 2-4, F_s is related to the surface tension coefficient (σ) and the

change in the droplet surface area (Δl). The σ is an intrinsic property of the precursor liquid prepared before the experiment. Droplets with higher σ values require a stronger electric field force to deform in the electric field. The surface area change is influenced by the frequency and extent of droplet breakup. As the droplet surface area decreases with further fragmentation, the surface tension increases correspondingly until it matches the F_e [20]. The expression is as follows:

$$F_s = \sigma \Delta l \tag{4}$$

The electrostatic repulsion force between droplets (F_r) is a force that varies with the electric field strength and the relative position of the droplets. This force can act either as a driving force or as a resistive force, particularly at locations where droplet accumulation is significant, such as near the nozzle. The expression for the F_r is given as follows:

$$F_r = \frac{K_e q_1 q_2}{r^2} \tag{5}$$

In addition to the aforementioned forces, the electrostatic spraying process also involves factors such as Saffman lift force. However, for the purposes of particle size calculation and process parameter optimization, such detailed and precise considerations are unnecessary. This study focuses on simulations under idealized conditions and employs orthogonal experimental design and controlled variable experiments to minimize errors.

The initial thrust is generated by the forward motion of the syringe pump. This force acts horizontally on the droplets, with the primary objective of propelling them toward the receiving plate. The magnitude of this thrust is solely dependent on the set flow rate, and the ejected droplets undergo uniformly accelerated linear motion. The expression for the force is as follows (where *a* represents the set acceleration):

$$F_I = ma (6)$$

The electrostatic spraying process occurs in a three-dimensional space, involving multiple directions. However, according to literature [17], this three-dimensional space is constructed from numerous repetitive two-dimensional planes. Therefore, in the experimental design of the electrostatic spraying process simulation, combined with practical considerations, this study will focus on the

central two-dimensional plane and perform force analysis on it. As mentioned in the previous section, the electrostatic force is the primary driving force for droplet motion, and its direction is inevitably toward the receiving plate (the end). Other forces directed toward the end include: initial thrust, electrostatic repulsion (in part), *etc*. Surface tension serves as the main opposing force, with additional opposing forces including: air resistance, and electrostatic repulsion [20] (in part). The details are illustrated in Figure 2.

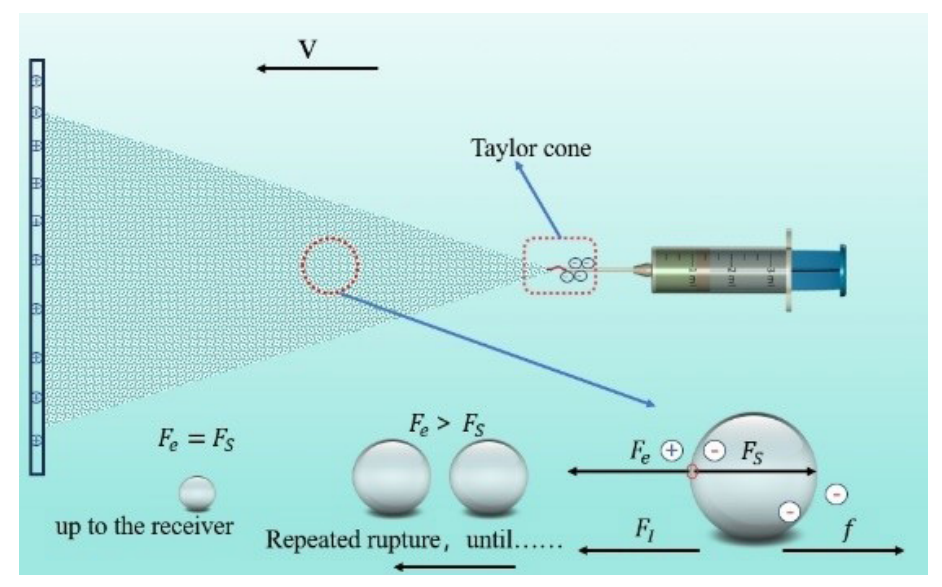


Figure 2. Electrostatic spray force analysis

The four forces shown in the figure can be roughly categorized into four directions. The direction of the forces determines the trajectory of the droplets in the electric field, while the magnitude of the forces governs the morphological changes of the droplets. In addition to the aforementioned horizontal forces, there are corresponding forces in the vertical direction as well. Gravity contributes to the weight of the droplet itself. The Saffman lift arises when there is a velocity difference between the particle and the surrounding fluid, with the velocity gradient of the fluid being perpendicular to the particle's motion direction. This creates a lift force directed from the low-speed side to the high-speed side due to the differing flow velocities on either side of the particle [25]. The electric field force arises because the receiving plate has a surface potential. Therefore, the droplet in the electric field is not subjected to the electric field force from a single point, but rather the total electric field force exerted by the

entire direction, which results in a resultant force. The combined analysis of the force field distribution, based on the magnitude and direction of each force, is a prerequisite for performing finite element simulation analysis [21].

Assuming the droplets are uniformly distributed in the electric field (ideal condition), when a droplet moves in a certain direction within the entire electric field, the sum of the electric field force and the initial thrust it experiences is greater than the sum of surface tension and air resistance, the droplet will break.

$$F_e + F_e > F_I + f \tag{7}$$

Based on Equations 1-3, 5 and 6, and considering the uniform distribution of the electric field, the electrostatic repulsive forces cancel each other out.

$$qe + ma > \sigma \Delta l + 6\pi \eta r v$$
 (8)

As the droplet breaks into smaller sizes, its surface tension increases with decreasing size, as analyzed below: Surface tension coefficient (σ) is the surface free energy per unit length, which serves to minimize the liquid's surface area. For a droplet, its total surface energy of the droplet (E_s), in J, is related to the σ be the surface tension coefficient of the liquid, in N/m, and the surface area (A), in m². The relationship between surface energy and surface tension is given by:

$$E_s + \sigma A \tag{9}$$

The surface area of a droplet is proportional to the square of its radius r, and the expression is:

$$A + 4\pi r^2 \tag{10}$$

The surface energy can be derived from the volume of the droplet (as opposed to the droplet diameter) and the density relationship. The volume V of the droplet is:

$$V = \frac{4}{3}\pi r^3 \tag{11}$$

Then the droplet mass can be expressed as:

$$m = \rho V = \rho \frac{4}{3}\pi r^3 \tag{12}$$

Therefore, the ratio of the surface area A to the radius r of the droplet can be expressed as:

$$\frac{A}{V} = \frac{4\pi r^2}{\frac{4}{3}\pi r^3} = \frac{3}{r} \tag{13}$$

This suggests that for the same volume of liquid, the smaller the droplet radius, the greater the surface area A/V per unit volume, and therefore the surface energy per unit mass.

In addition, pressure can also explain this phenomenon. In droplets, surface tension causes an additional pressure inside the liquid (Laplace pressure), which is determined by surface tension and curvature [22]:

$$\Delta \rho = \frac{2\sigma}{r} \tag{14}$$

The smaller the droplet, the smaller its radius r, resulting in a larger differential pressure ΔP . The increased surface tension effect will affect the behavior of the droplets more significantly. These formulations show that as the droplets become smaller, the effect of surface tension gradually becomes dominant, affecting the stability and rupture behavior of the droplets. Occurs when a certain value is reached [23]:

$$qe + ma \le \sigma \Delta l + 6\pi \eta r v \tag{15}$$

Based on the ideal situation, considering that the droplet has been broken several times and the mass is ignored, the η is calculated as 0.01809 mPa·s at 20 °C, and the π is 3.14159, the droplet radius and velocity can be obtained by simulation, and Δ the droplet radius and velocity can be obtained by simulation according to the droplet radius change of the simulated data twice, combined with Equation 10, then the critical point of the surface tension of the droplet crushing is:

$$\sigma = \frac{qE + 0.34rv}{\Delta l} \tag{16}$$

2.2 Set the relevant parameters

A 2D model is established using ANSYS finite element analysis software. The electrostatic spraying system is an axisymmetric system. To simplify the model and reduce computational load without compromising calculation accuracy, a 2D

model is selected for the analysis of the coaxial electrospinning electric field. In the electrostatic spraying process, the high-voltage power supply acts as the driving force for spraying and generates a high-voltage electric field between the nozzle and the receiving device. Therefore, the electrostatic spraying electric field model primarily includes the nozzle, the air medium between the nozzle and the receiving device, and the receiving device. The coaxial electrospinning electric field model established based on the actual problem description is shown in Figure 3. The nozzle diameter is 0.3, and the nozzle wall thickness is 0.1. The thickness of the receiving device (tin foil) is 0.1.

The multiphase flow model includes: Discrete Phase Model (DPM), Volume of Fluid (VOF), and Euler-Lagrange method. The DPM is used to simulate droplet generation, motion, and evaporation, suitable for droplets with a well-defined particle size distribution. The VOF method is used to simulate the dynamic changes at the liquid-gas interface, ideal for simulating droplet generation and breakup. The Euler-Lagrange method describes the combined dynamics of the gas phase and liquid phase.

Important parameter settings include liquid density ρ (kg/m³), viscosity μ (Pa·s), surface tension coefficient σ (N/m), and the density and viscosity of the surrounding gas (e.g. air: $\rho = 1.225$ kg/m³, $\eta = 1.81 \times 10^{-5}$ Pa·s). Additionally, the flow velocity and direction of the gas are specified.

To incorporate the electric field model in ANSYS, the electric field module must be activated, and the electrostatic field calculation mode (based on the Poisson equation [24]) must be selected. According to the potential field equation, the initial charge of the droplet (in C) is typically calculated based on experiments or Equation 18.

$$\nabla^2 \varphi = -\frac{\rho_e}{\varepsilon} \tag{17}$$

where φ represents the electric potential, ρ_e is the charge density, ε is the dielectric constant,

$$q = \frac{8\pi\varepsilon r^2 E}{k} \tag{18}$$

where r is the droplet radius, and (E) is the electric field intensity. After determining these values, boundary conditions need to be specified, including:

- nozzle outlet voltage: the high voltage of the nozzle is specified (e.g. 8-12 kV in this study),
- collector voltage: the collector is assigned a zero potential or is grounded,

 electric field distribution: the electric field strength and direction between the nozzle and the collector are defined.

Additionally, in the droplet generation and motion setup (*i.e.* the injection source setup), the initial conditions should be specified as follows:

- droplet diameter range: the particle size distribution during droplet generation,
- generation rate: the liquid flow rate at the nozzle (e.g. 0.1 to 1 m/s),
- initial droplet position: At the nozzle outlet.

2.3 Simulation analysis and discussion of results

2.3.1 Orthogonal design of experiments

This study establishes a 3-factor, 3-level orthogonal experiment. Based on the variables that can be practically controlled in the model (*i.e.* flow rate, receiving distance, and voltage), the factors are established. Finally, the droplet size, motion velocity in the electric field, and the maximum residence time of the droplet in the electric field are scored based on the results of the simulation. The simulation process analyzes the conditions within 100 s after injection. The orthogonal experimental design Table 1.

Table 1. Offilogoliai Ca	speriment table				
Factor	Unit	Level			
racioi	Unit	1	2	3	
Voltage	[kV]	8	10	12	
Accept the distance	[cm]	20	25	30	
Velocity of flow	[mI /min]	0.1	0.2	0.3	

Table 1. Orthogonal experiment table

After the simulation, histograms of particle diameter, particle velocity, and residence time are plotted against the factors to analyze the simulation results. By examining key indicators such as particle diameter, particle velocity, residence time, and voltage, the performance and effectiveness of the spraying process can be evaluated. Table 2 represents the different process settings for each group.

 Table 2.
 Table of orthogonal experimental serial numbers

Group number	Factor			
number	1	2	3	
1	1	1	1	
2	1	2	3	
3	1	3	2	

Group number	Factor			
number	1	2	3	
4	2	2	1	
5	2	1	2	
6	2	3	3	
7	3	3	1	
8	3	2	2	
9	3	1	3	

2.3.2 Orthogonal experimental results

The simulation is conducted based on the orthogonal experiments designed in Tables 1 and 2. Histograms are plotted based on the simulation results. In this section the nine sets of data have been analyzed and discussed.

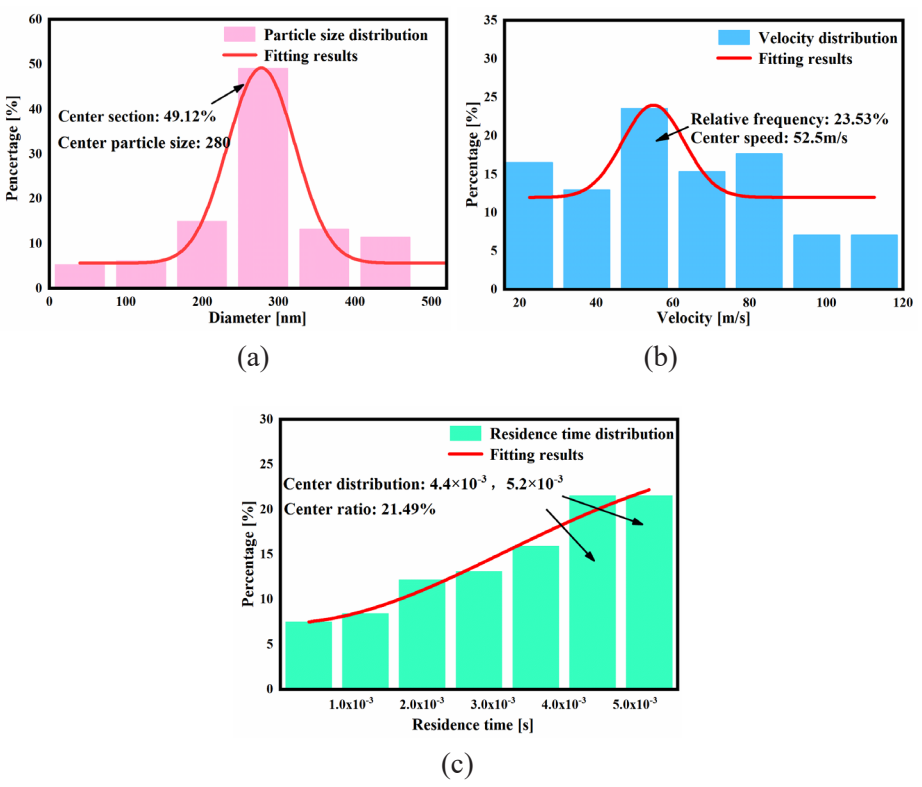
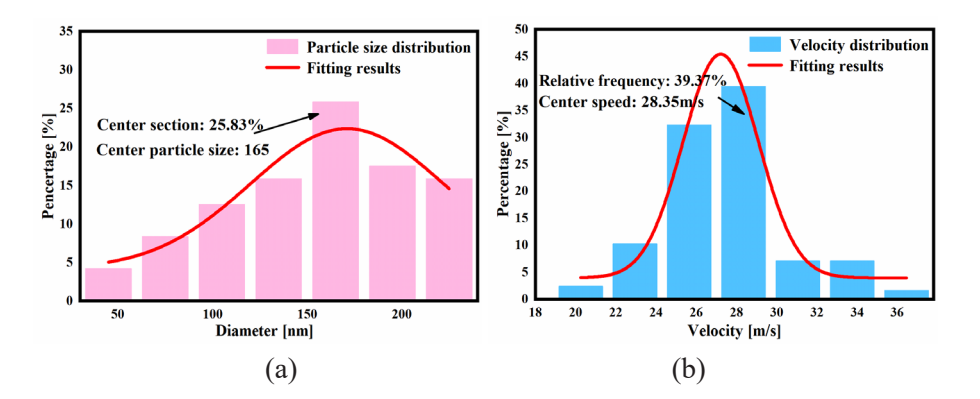


Figure 3. The set of simulation results for Group 1: a histogram of particle size distribution (a), a histogram of velocity distribution (b) and a histogram of residence time distribution (c)

For experimental group 1, the process conditions were set at a voltage of 8 kV, a receiving distance of 20 cm, and flow rate of 0.1 mL/min. According to the particle size distribution histogram in Figure 3(a), the particle size are approximately distributed between 0 and 500 nm. The nonlinear Gaussian fitting curve indicates that the particle size distribution approximates a near-normal distribution, peaking around 280 nm, which accounts for 49.12% of particles. This phenomenon suggests that the droplets undergo minimal fragmentation in the electric field, achieving a minimum size of around 100 nm. However, due to experimental parameters such as voltage, receiving distance, and flow rate, not all droplets are fragmented to this extent.

Figure 3(b) presents the velocity distribution histogram, with values concentrated between 20 and 120 m/s. However, the velocity distribution is non-uniform. The largest proportion of the distribution does not fall in the centre of the x-axis, so the Gaussian fit is only moderate. The most common velocity is 52.5 m/s, accounting for approximately 23.53%. The velocity does not exhibit significant fluctuations, indicating that no droplet escape or stalling phenomena are observed in this group. Figure 3(c) shows the histogram of the residence time distribution, with calues from 1×10^{-3} to 5×10^{-3} s. The distribution generally shows an overall increasing trend, with two distinct peaks at 4.4×10^{-3} and 5.2×10^{-3} s, each accounting for 21.49%. In summary, the first experimental group shows a normal distribution of particle size, no significant escape or stalling, and the simulation condition is considered to be quite favourable.



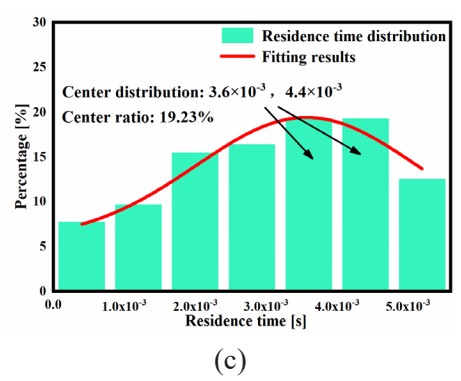


Figure 4. The set of simulation results for Group 2: a histogram of particle size distribution (a), a histogram of velocity distribution (b) and a histogram of residence time distribution (c)

The process conditions for Group 2 were set a voltage 8 kV, receiving distance 25 cm, and flow rate 0.3 mL/min. According to the particle size distribution histogram in Figure 4(a), the distribution for this group ranges from 50 to 250 nm, with a concentration around 165 nm, accounting for 25.83%. However, the particle size distribution in this group is not a uniform normal distribution. The Gaussian fit curve is relatively flat, and most of the distribution is concentrated above 150 nm.

Figure 4(b) displays the histogram of the velocity distribution. The velocity range is between 20 and 36 m/s, and the velocity distribution follows a normal distribution with a suitable Gaussian fit. Most of the velocities are concentrated around 28.35 m/s, accounting for 39.37%. It is noted that the velocity concentration in this group is high, with the velocity distribution at 26 m/s only slightly below the highest value, while both low and high-speed distributions are rare. This concentrated velocity distribution is also reflected in the residence time distribution in Figure 4(c). The residence time distribution ranges from 0 to 5×10^{-3} s, with residence times of 3.6×10^{-3} and 4.4×10^{-3} s each accounting for 19.23%. The total of seven data groups have relatively small differences, indicating that the motion trajectories of the droplets in the electric field are very uniform. This uniformity may be related to the increased total motion distance and the higher initial flow rate. However, compared to Group 1 (see Figure 3), the speed in this group has decreased significantly. If the particle size reduction is due to a higher degree of droplet fragmentation, the relative decrease in velocity indeed corroborates this trend.

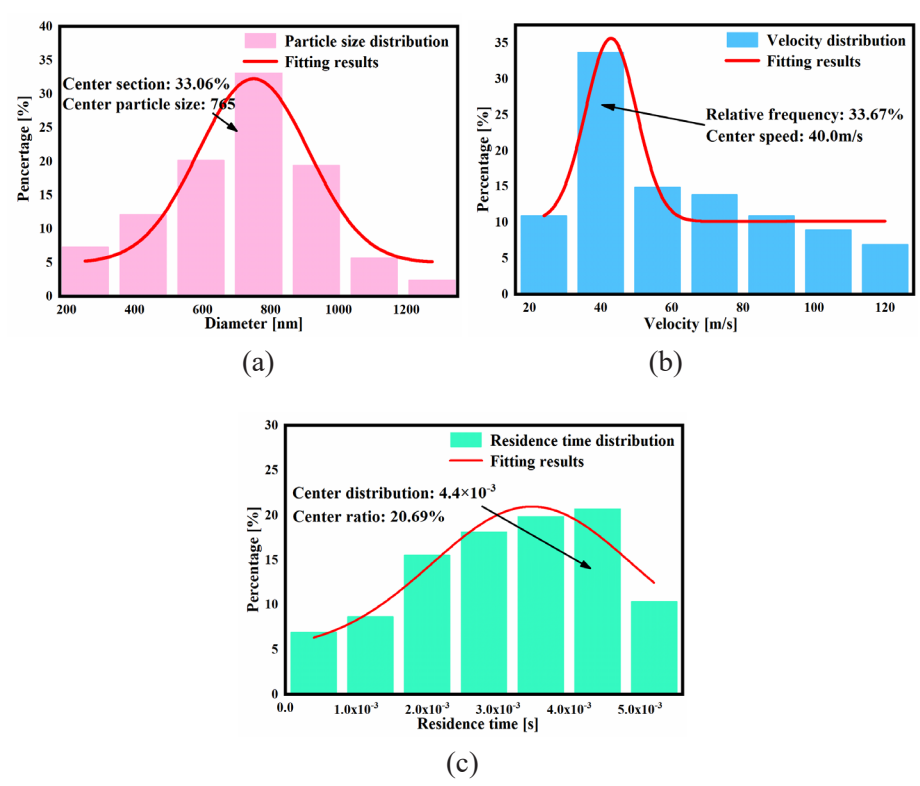


Figure 5. The set of simulation results for Group 3: a histogram of particle size distribution (a), a histogram of velocity distribution (b) and a histogram of residence time distribution (c)

The process conditions for Group 3 were voltage 8 kV, receiving distance 30 cm, and flow rate 0.2 mL/min. From the particle size distribution histogram in Figure 5(a), it can be seen that the particle size for this group ranges from 200 nm to 1200 nm, with the majority concentrated around 765 nm, accounting for about 33.06%. Based on the Gaussian fit curve, the particle size distribution follows a regular normal distribution. The particle sizes at 600 and 900 nm are relatively balanced, with fewer particles as the size moves towards either extreme.

Figure 5(b) shows the histogram of the velocity distribution, which has a moderate Gaussian fit. The velocity range is between 20 and 120 m/s, with most of the velocities concentrated around 40 m/s, accounting for about 33.67%. However, the concentration is skewed to the left, not centred, and after exceeding 40 m/s, the velocity gradually decreases in a stepwise fashion. Figure 5(c) shows the residence time distribution, which ranges from 0 to 5×10^{-3} s. It starts at 0 and

steadily increases until the residence time reaches 4.4×10^{-3} s, after which a few droplets have a residence time around 5×10^{-3} s. The most widely distributed residence time is 4.4×10^{-3} s, accounting for 20.69%. The distribution in this group is relatively uniform, with a moderate Gaussian fit. Overall, the particle size distribution in the third group follows a normal distribution, the velocity is within a certain range, and there are no significant stalling issues. The simulation results are relatively good.

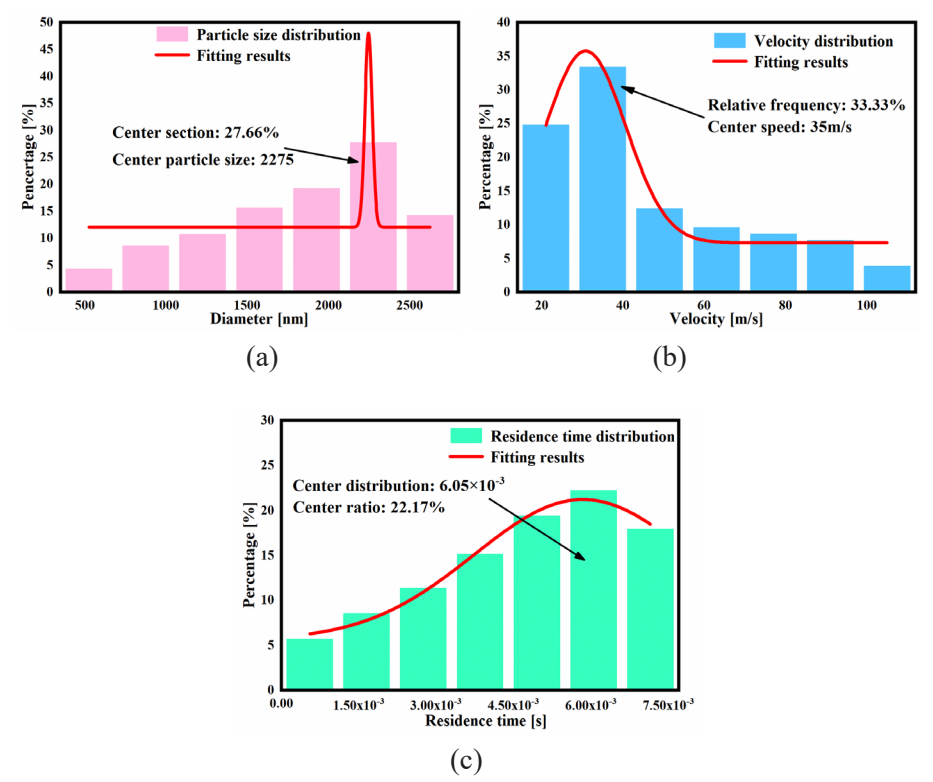
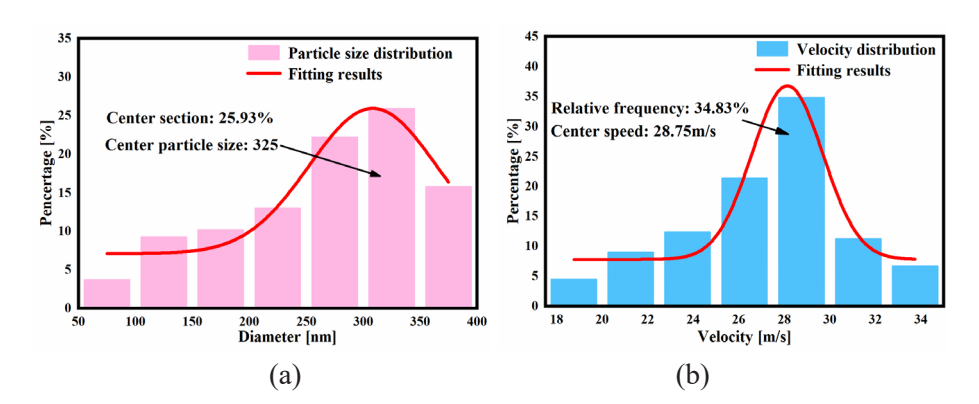


Figure 6. The set of simulation results for Group 4: a histogram of particle size distribution (a), a histogram of velocity distribution (b) and a histogram of residence time distribution (c)

The process conditions for Group 4 were set at a voltage 10 kV, receiving distance 25 cm, and flow rate 0.2 mL/min. The particle size distribution histogram in Figure 6(a) is shown that the particle size range is approximately 500-2500 nm. The distribution is concentrated on the larger particle size side, around 2275 nm, accounting for 27.66%. According to the simulation results,

the particle size distribution increases stepwise from a minimum value of 500 to about 2000 nm, then sharply decreases after reaching the maximum value around 2275 nm, showing an irregular distribution pattern. The Gaussian fitting also indicates a poor fit for this group.

Figure 6(b) presents the velocity distribution histogram. While the velocity distribution in this group generally follows the same trend as that of the third group, it covers a broader range of speeds. The peak velocity is around 35 m/s, accounting for 33.33%, while the 20 m/s velocity also accounts for a significant portion (25%). Cumulatively, velocity between 20 and 40 m/s accounts for more than 50% of the distribution. The concentration of velocity suggests that the droplets in the electric field follow similar trajectories, resulting in similar force conditions and nearly identical velocities. Figure 6(c) shows the residence time distribution, which ranges from 0 to 7.5×10⁻³ s. The most prevalent residence time is around 6.05×10⁻³ s, accounting for 22.17% of cases. The residence time increases progressively from 0, exhibiting a very smooth growth trend, with a considerable portion of droplets reaching residence time near 7.5×10^{-3} s. Although the particle size distribution in this group is concentrated on the larger size range, the overall trend remains within normal bounds. Furthermore, the velocity distribution provides no evidence of significant escape or stalling phenomena.



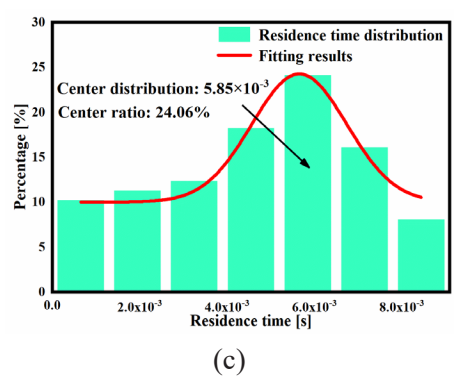


Figure 7. The set of simulation results for Group 5: a histogram of particle size distribution (a), a histogram of velocity distribution (b) and a histogram of residence time distribution (c)

For the experimental Group 5, the process conditions were set at a voltage of 10 kV, a receiving distance of 20 cm, and a flow rate of 0.2 mL/min. As shown in Figure 7(a), the particle size distribution ranges from 50 to 400 nm, peaking around 325 nm, which accounts for approximately 25.93% of particles. Notably, over 60% of the distribution falls within the larger particle size range. The Gaussian fitting is moderate, indicating the overall particle size is relatively small. Figure 7(b) presents the velocity distribution histogram. The velocity with the widest distribution is around 28.75 m/s, accounting for 34.83%. Although the peak distribution is not centered, the relatively large proportions in the dominant regions lead to a better Gaussian fitting. The velocity distribution around 26 m/s also shows a notable proportion, exceeding 20%. Therefore, the velocity distribution in this group is considered well-behaved. The residence time distribution, as depicted in Figure 7(c), shows that 24.06% of the droplets have a residence time around 5.85×10⁻³ s. Similar to the velocity distribution, the most widely distributed residence time is not centered, but the variation remains insignificant, especially in the range from 0 to 4×10^{-3} s. For this fifth group, although the particle size distribution fitting is not optimal, both the velocity and residence time are effectively controlled within certain ranges. Overall, the performance of the simulation is satisfactory.

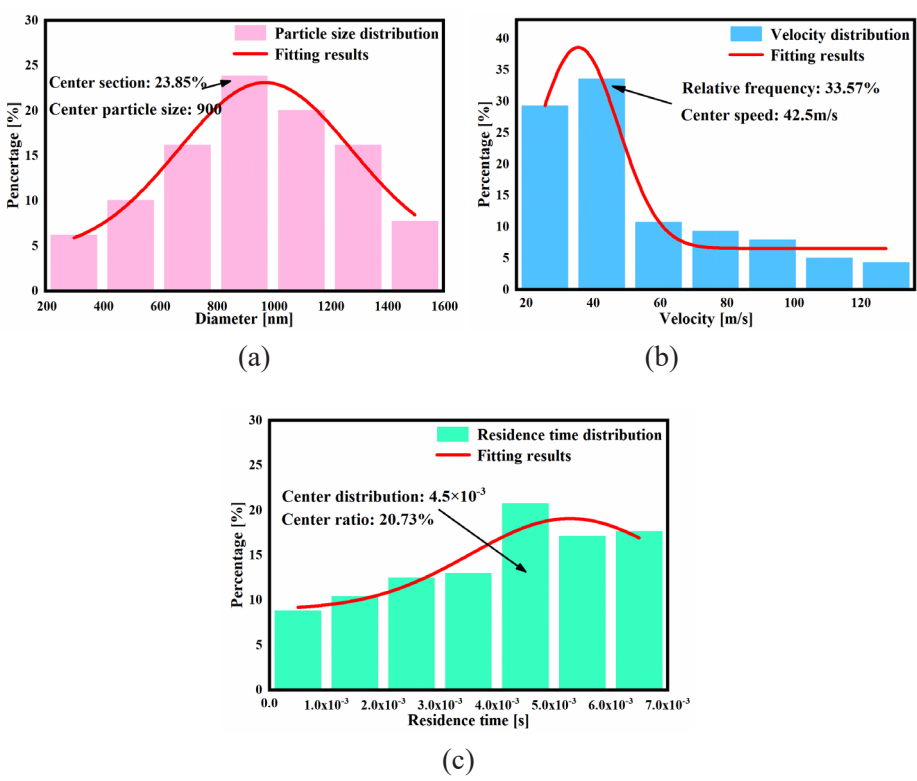


Figure 8. The set of simulation results for Group 6: a histogram of particle size distribution (a), a histogram of velocity distribution (b) and a histogram of residence time distribution (c)

The process conditions for Group 6 were set to a voltage of 10 kV, a receiving distance of 30 cm, and a flow rate of 0.3 mL/min. In Figure 8(a), which displays the particle size distribution histogram, the modal distribution occurs around 900 nm, accounting for 23.85% of particles. The Gaussian fitting curve indicates an approximately normal distribution, with the peak at the center position. The distribution increases progressively from around 200 nm to the center peak at 900 nm, showing a very regular pattern. Figure 8(b) shows the velocity distribution histogram. The velocity distribution ranges from 20 to 120 m/s with predominant values in the lower velocity range. The most frequent velocity is around 42.5 m/s, accounting for 33.57% of cases. The distribution between 20 and 42.5 m/s (the low-speed range) occupies nearly 70%, with no abnormal phenomena such as stalling. Figure 8(c) illustrates the residence time distribution histogram. The peak distribution occurs around 4.5×10⁻³ s,

accounting for 20.73%, while the remaining distributions are relatively uniform, ranging between 10% and 20%. Although the distribution is uniform, the fitting quality is not optimal. Overall, the particle size distribution in the sixth group is quite good, with no abnormal situations observed. The simulation results for this group are favorable.

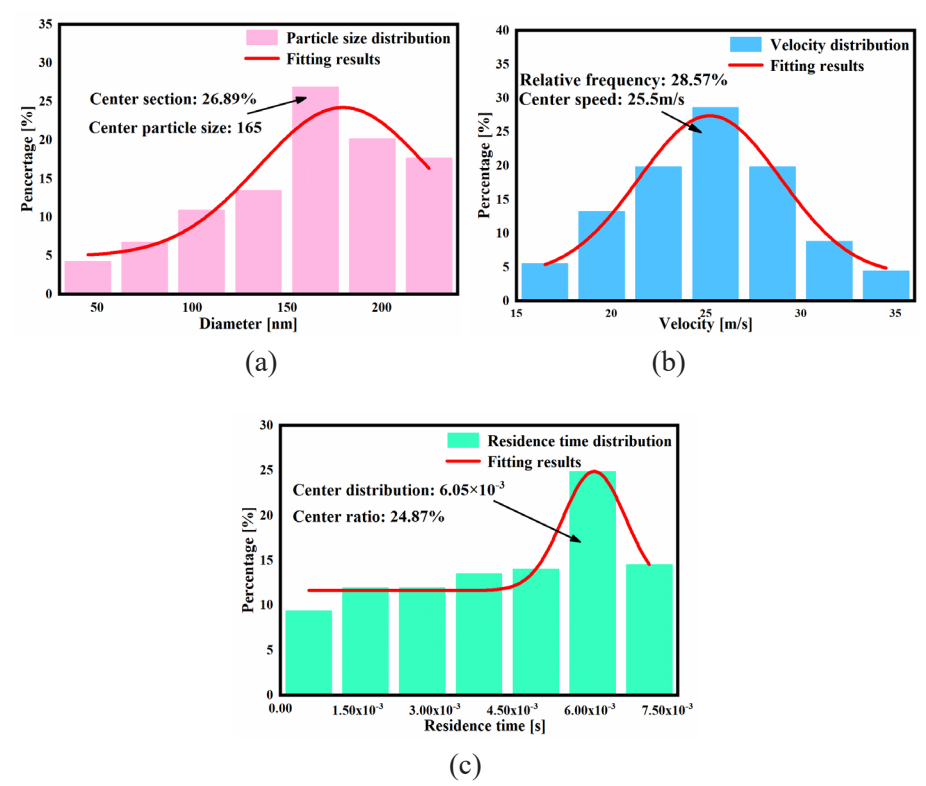


Figure 9. The set of simulation results for Group 7: a histogram of particle size distribution (a), a histogram of velocity distribution (b) and a histogram of residence time distribution (c)

The process conditions for Group 7 were set at a voltage of 12 kV, a receiving distance of 30 cm, and a flow rate of 0.1 mL/min. Figure 9(a) shows the particle size distribution histogram, with the distribution range between 50 and 250 nm. The broadest distribution is around 165 nm, accounting for 26.89%. The particle size distribution is mainly concentrated in the larger size range, with over 60% of the distribution above 150 nm. As a result, the Gaussian fitting is not very high, but the overall range of the distribution is in the small particle size range.

Figure 9(b) presents the velocity distribution histogram, which follows a regular normal distribution. The overall range is between 15 and 35 m/s, with the broadest distribution around 25.5 m/s, accounting for 28.57%, and this value is centered, resulting in a high fitting degree. Figure 9(c) shows the residence time distribution histogram, which ranges from 0 to 7.5×10^{-3} s. The highest proportion occurs at 6.05×10^{-3} s, accounting for 24.87%. Aside from this peak, the other residence time distributions are relatively uniform, mostly ranging between 10% and 15%. Overall, the distribution in the seventh group is normal, and the simulation results are good.

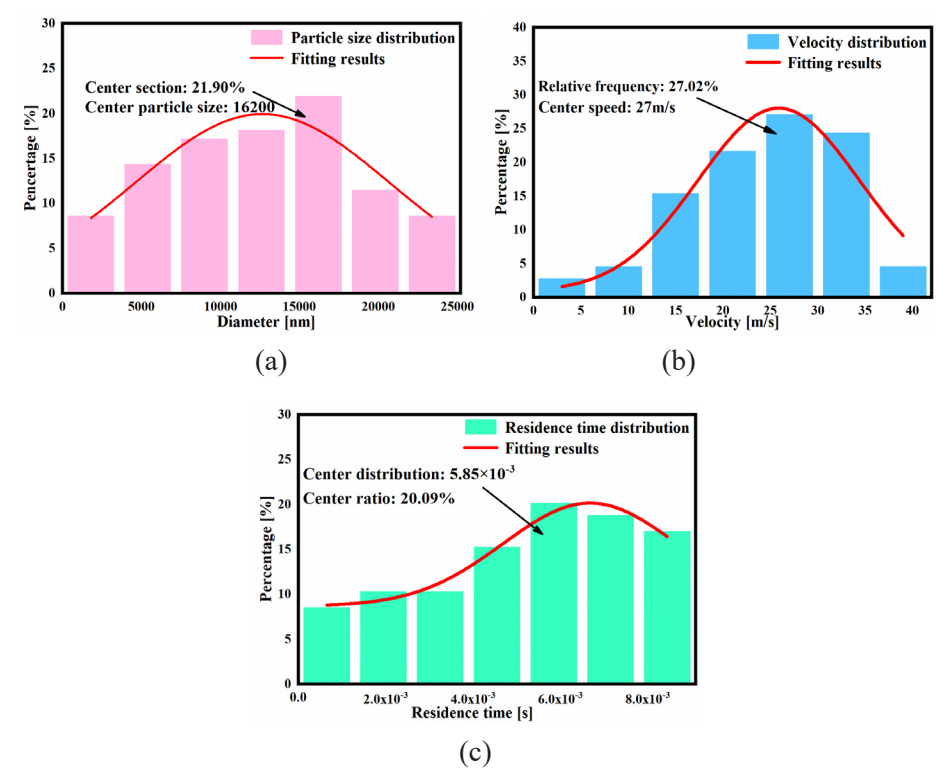


Figure 10. The set of simulation results for Group 8: a histogram of particle size distribution (a), a histogram of velocity distribution (b) and a histogram of residence time distribution (c)

The process conditions for Group 8 were set at a voltage 12 kV, receiving distance 25 cm, and flow rate 0.2 mL/min. Figure 10(a) shows the particle size distribution histogram, with the distribution range spanning from 0 to 25,000 nm. The broadest distribution is around 16,200 nm, accounting for 21.90%, and is

slightly to the right of the center. The Gaussian fitting degree is not high, and the particle size range is very large, with the maximum particle size around 25,000 nm. Considering the overall simulation results, this suggests that there might be issues with droplet fragmentation, leading to larger particle sizes. Figure 10(b) presents the velocity distribution histogram, which ranges from 1 to 40 m/s. The broadest distribution is similarly to the right of the center, with the most frequent velocity around 27 m/s, accounting for 27.02%. The distribution between 25 and 35 m/s accounts for more than 50%, but the fitting degree is also not very high. Figure 10(c) shows the residence time distribution, which is relatively uniform. Two residence times share the highest proportion, both at 17.17%, for 3.15×10^{-3} and 2.45×10^{-3} s. The Gaussian fitting degree is low. Although the simulation results for the eighth group do not show large deviations, the fitting degree of the data is generally poor, and the particle size is large. This suggests that the fragmentation of the droplets might not be sufficient.

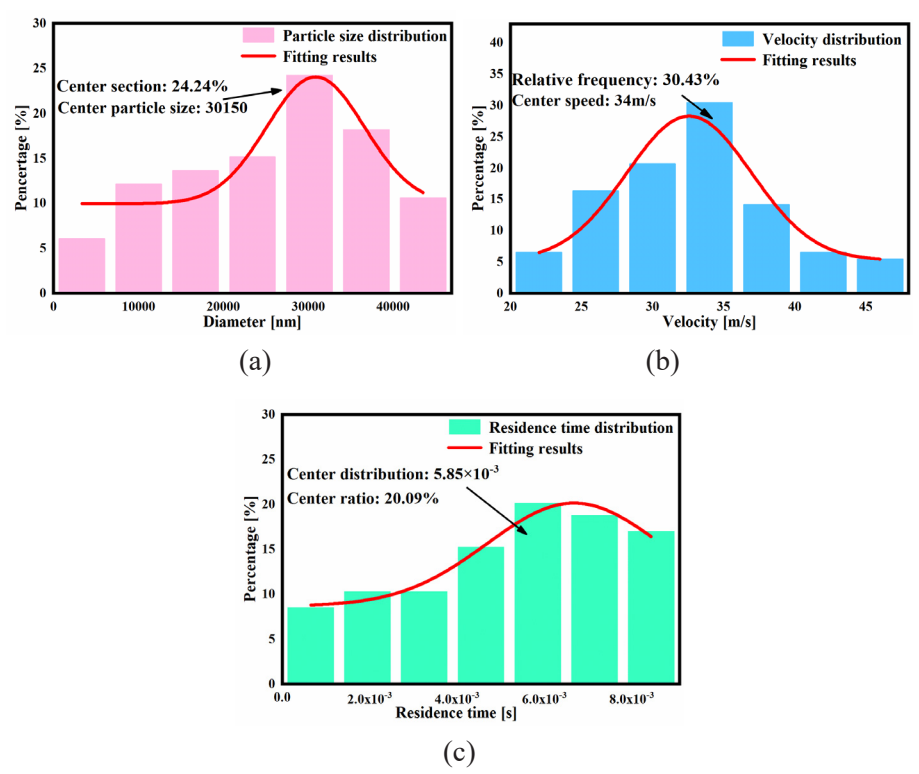


Figure 11. The set of simulation results for Group 9: a histogram of particle size distribution (a), a histogram of velocity distribution (b) and a histogram of residence time distribution (c)

The process conditions for Group 9 were set at a voltage 12 kV, receiving distance 20 cm, and flow rate 0.3 mL/min. Figure 11(a) shows the particle size distribution histogram, with the distribution range spanning from 0 to 40,000 nm. The broadest distribution is around 30,150 nm, accounting for 24.24%, and is slightly to the right of the center. The Gaussian fitting degree is not high, and the particle size range is very large. Compared to the eighth group, this group shows an even larger particle size distribution, which, considering the overall simulation results, suggests that there might be an issue with droplet fragmentation, leading to larger particle sizes. Figure 11(b) presents the velocity distribution histogram, which fits well and shows a nearly normal distribution. The distribution range is from 20 to 45 m/s, with the broadest distribution around 34 m/s, accounting for 30.43%. Figure 11(c) shows the residence time distribution histogram, with a range from 1 to 8×10⁻³ s. The broadest distribution occurs at 5.85×10⁻³ s, accounting for 20.09%, and the remaining distributions are relatively uniform with little variation. Overall, the ninth group has an excessively large particle size distribution range, with the maximum reaching 40 µm. This indicates that the droplet fragmentation is insufficient, leading to suboptimal simulation results. Based on the results of the nine simulated experiments, the following orthogonal experiment scoring table can be compiled:

Table 3. Orthogonal experiment scoring scale

Number	A	В	С	Residence time [s]	Diameter [m]	Velocity [m·s ⁻¹]	Score
1	1	1	1	5.5e-3	47.7	34.1	88
2	1	3	2	5.0e-3	256	197	93
3	1	2	3	5.0e-3	136	85.1	95
4	2	2	1	7.14e-3	22.6	105	85
5	2	1	2	8.5e-3	36.5	34.0	86
6	2	3	3	6.7e-3	146	128	92
7	3	3	1	8.5e-3	22.6	33.4	86
8	3	2	2	5e-4	29.6	37	96
9	3	1	3	7.5e-3	4560	46.1	93
K1	2.76	2.67	2.59	_	_	_	_
K2	2.63	2.66	2.75	_	_	_	_
K3	2.75	2.71	2.80	_	_	_	_
R	0.13	0.05	0.21	_	_	_	_
Factors of priority		CAB					
Optimize the solution			$A_3B_2C_2$				

Based on the results from the orthogonal experiment scoring table, the primary factors affecting the electrostatic spraying process are flow rate (C), voltage (A), and distance (B) in that order (CAB). The optimized process parameters are: voltage is 12 kV, distance is 25 cm, and flow rate is 0.2 mL/min.

2.3.3 Simulation analysis of control variables

The law of influence of flow velocity is shown in Figure 12. Figure 12(a) illustrates the relationship between flow rate and particle size. The blue line (with points) shows that as the flow rate increases, the particle size decreases. However, at approximately 0.14 mL/min, the rate of decrease in particle size begins to slow down, resulting in the lower linear fitting accuracy. The red line represents the linear fit for the flow rate and particle size relationship, with the equation: y = -65092.86x + 12927.1. This equation provides an approximate way to calculate the particle size at a given flow rate within the experimental range. Figure 12(b) shows the relationship between flow rate and droplets velocity in the electric field. It is evident that as the flow rate increases, the velocity of the droplets also increases. However, similar to the particle size trend, this upward slope starts to decelerate around a flow rate of 0.14 mL/min. According to Equation 7, the greater the initial thrust, the more frequently the droplets are likely to break up in the electrostatic field, leading to a reduction in particle size. This change in velocity and particle size occurs simultaneously around 0.14 mL/min, suggesting a point where the dynamics of the spraying process change. Figure 12(c) displays the distribution of residence time, presenting only the longest residence time values. By observing the relationship between residence time and velocity, it can be inferred whether the droplets deviate from their expected trajectory in the electrostatic field. The narrow flow rate range in this figure suggests that the droplet movements is relatively stable and predictable. Collectively, this experiment shows how key process parameters, particularly flow rate, influence particle size, velocity, and residence time of droplets, with a critical transition occurring at 0.14 mL/min that alters the spraying dynamics.

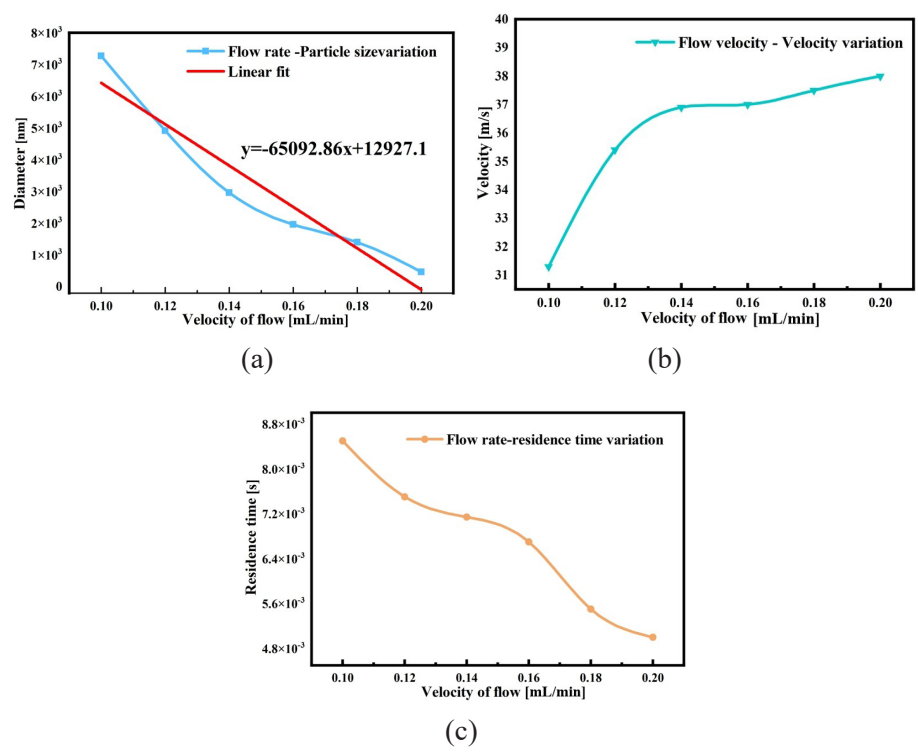
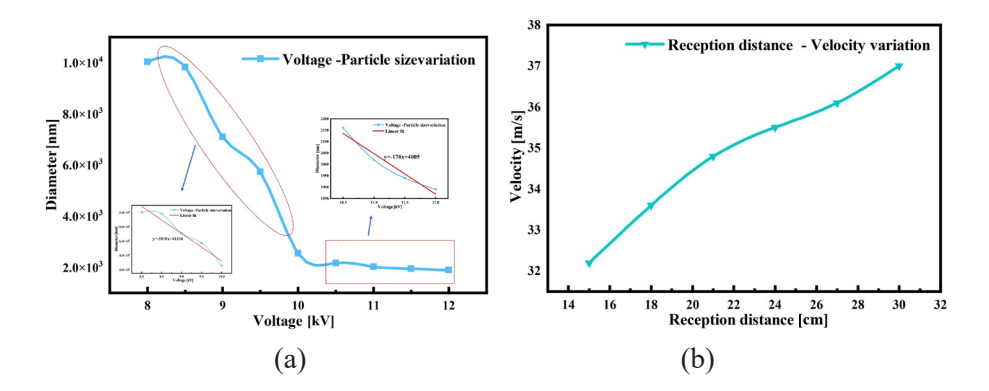


Figure 12. Flow velocity influence law diagram: flow velocity-particle size diagram (a), flow velocity-velocity relationship diagram (b) and flow velocity-residence time relationship diagram (c)

The law of influence of voltage is shown in Figure 13. Figure 13(a) shows the relationship between particle size and voltage in the range of 7.5 to 12 kV. Since there is a significant change in particle size behavior at 10 kV, the relationship between particle size and voltage can be discussed in two phases. In the first phase, as the voltage increases, the particle size decreases sharply, ranging between 2×10^3 and 1×10^4 nm. According to Equation 7, the electric field force, which is the dominant force in the electrostatic field, is the primary cause of droplet breakup. As the voltage increases, the electric field force increases, leading to more frequent droplet breakup and thus smaller particle sizes. The linear fit equation for this phase is y = -3810x + 41336. After reaching 10 kV, the rate of decrease in particle size slows significantly, and the particle size stabilizes between 1850 and 2200 nm. Clearly, the trend in the second phase is much flatter compared to the first phase, which is why the change is difficult to discern in the overall plot. The linear fit equation for this second phase is y = -178x + 4005. The

difference in slopes between the two phases is 3632, reflecting the distinct change in the relationship between voltage and particle size. Figure 13(b) illustrates the relationship between voltage and droplet velocity. As the voltage increases, the droplet velocity in the electric field also increases. The increasing electric field force, acting as the net force, accelerates the droplets toward the collection plate. Similar to the particle size trend, at 10 kV, there is a noticeable shift in the rate of velocity increase, though it soon returns to a more gradual trend This change can be explained by Equation 9, where smaller droplets exhibit higher surface tension. The increased surface tension partially counteracts the electric field force, leading to velocity stabilization. Overall, the marked change in velocity confirms that voltage is a major factor affecting the droplet's movement. Figure 13(c) shows the relationship between voltage and residence time. As the voltage increases, the residence time steadily decreases, eventually reaching a minimum value of around 1×10⁻³ s, after which it stabilizes. The reduction in residence time correlates with the increase in droplet velocity, as faster droplets spend less time in the field. Notably, the residence time exhibits no significant deviations, indicating that the droplets follow a consistent trajectory without any major disruptions. In summary, voltage critically influences both the particle size and droplets velocity, with a noticeable behavioral shift occurring at 10 kV. While the surface tension of smaller droplets acts to counterbalance the increased electric field force, the overall trends indicate that voltage is a dominant factor influencing droplet dynamics.



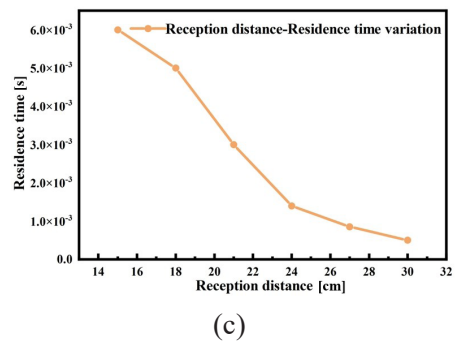


Figure 13. Voltage influence law diagram: voltage-particle size relationship diagram (a), voltage-velocity relationship diagram (b) and voltage-residence time relationship diagram (c)

Reception distance affects the law is shown in Figure 14. Figure 14(a) shows the relationship between the collection distance and particle size. It is evident that as the collection distance increases, the particle size gradually decreases. The fit curve does not demonstrate a high level of accuracy, and trend changes occur at distances of 18, 20 and 24 cm. The approximate fit equation for this relationship is: y = -719.62x + 22858.1. This equation can roughly describe the particle size at a certain location in the electric field, indicating that an increase in distance leads to a reduction in particle size. However, the trend is not linear, and the observed variations at specific distances indicate complex interactions at these points. Figure 14(b) depicts the relationship between the collection distance and droplet velocity. As the collection distance increases, the velocity generally rises, but the rate of increase diminishes between 32 and 38 m/s, indicating that the collection distance has a minimal effect on the velocity within this range. A noticeable trend shift occurs around 20 to 24 cm, implying that beyond a certain distance, the collection distance's influence on velocity becomes less significant. Figure 14(c) shows the relationship between the collection distance and residence time. The trend here mirrors that in Figure 13(c), suggesting that the collection distance likely has less influence on residence time compared to other factors such as flow rate. The curve is not smooth, primarily due to the scattered distribution of the data points indicating that additional factors may combine with collection distance to affect residence time. In summary, the collection distance plays an important role in influencing particle size and droplet velocity, with a more noticeable effect on particle size. However, the relationship is not strictly linear, and trend shifts at specific distances suggest that the electric field's impact on the droplets changes as the collection distance increases. The residence time, however, seems to be more influenced by other factors like flow rate than by the collection distance.

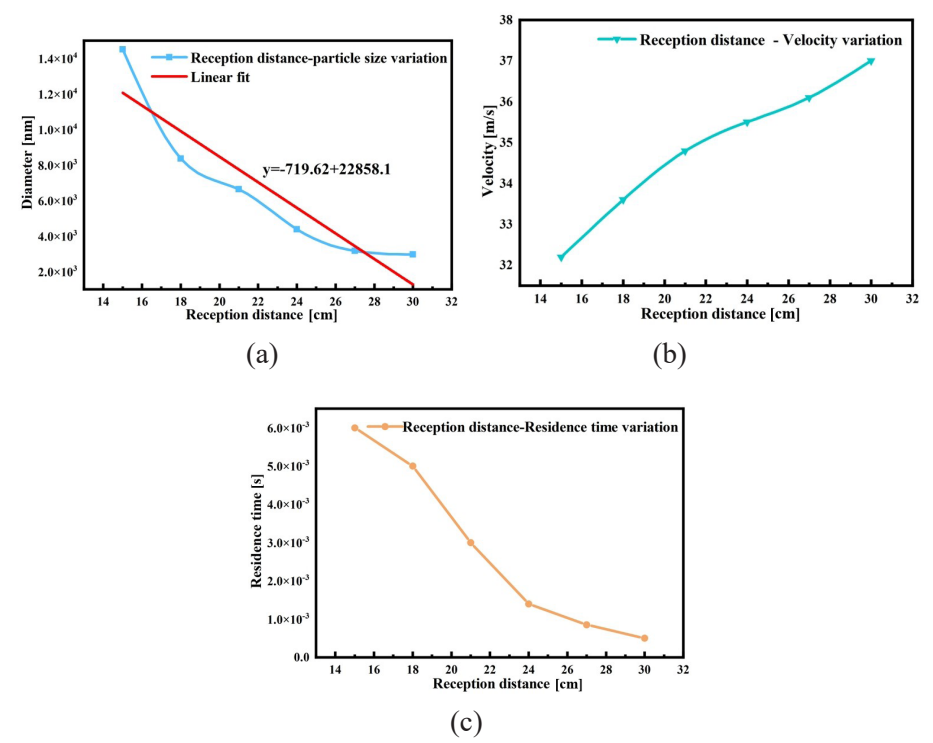


Figure 14. Reception distance law diagram: acceptance distance-particle size (a), acceptance distance-velocity (b) and acceptance distance-residence time (c)

3 Experimental Part

3.1 Materials

HNO₃·3H₂O, acetone, ethylenediamine, ethyl acetate and DMF were purchased from Chengdu Kelong Chemical Co., Ltd. Deionized water was lab-made. Al powder (100 nm) and CuO (100 nm) powder were obtained from Shanghai Rice Material Technology Co., Ltd. F₂₃₁₁ and PVP were provided by Zhonghao Chenguang Chemical Research Institute. Cu-en powder was prepared according to Ref. [16].

3.2 Preparation of samples

The preparation process of Cu-en was presented in Figure 15. In a typical Cu-en preparation process, a certain mass of copper nitrate is dissolved in deionized water to form a stable solution with a concentration of 2 mol/L. And then, the copper sulfate solution is mixed evenly with ethylenediamine, and anhydrous ethanol is added to the mixture slowly. Finally, the product Cu-en is obtained by drying at 50 °C for 7 days.





Figure 15. The preparation schematic illustration of Cu-en

The preparation process of Al/CuO/Cu-en composites by electrostatic spraying method was presented in Figure 16. For a typical fabricating process, 2-3% F₂₃₁₁, 15% Cu-en and 1% PVP were dissolved in DMF to form a clear solution. Then, a specific amount of Al and CuO were added into the above solution. The mixture was ultrasonically mixed for 45 min to allow the particles to disperse homogeneously. This was followed by an additional 24 h of magnetic stirring at room temperature. Finally, the precursor solution was added into a syringe and secured for electrostatic spraying. In the process of electrostatic spraying, 12 kV potential was attached to the needle using a high-voltage-power supply. The flow was set at 0.2 mL/min. The composites were collected on the aluminum foil situated at 25 cm from the needle.

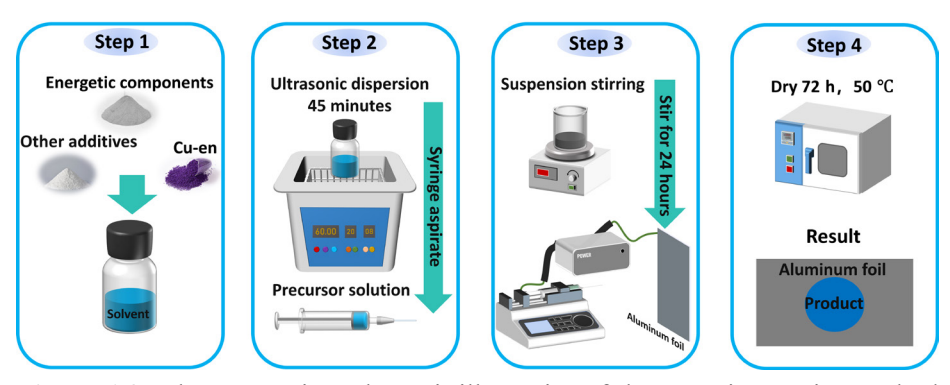


Figure 16. The preparation schematic illustration of electrostatic spraying method

The preparation process of Al/CuO/Cu-en composites by solvent evaporation method was presented in Figure 16. For a typical fabricating process, 2-3% F_{2311} and 1% PVP were dissolved in DMF to form a clear solution. Then, a specific amount of Al and CuO were added into the above solution. The mixture was ultrasonically mixed for 45 min to allow the particles to disperse homogeneously. Cu-en is added to a small amount of deionized water to prepare a Cu-en solution. The Cu-en solution is added to a continuously stirred and heated suspension, and the solids are removed after the solvent has completely evaporated.

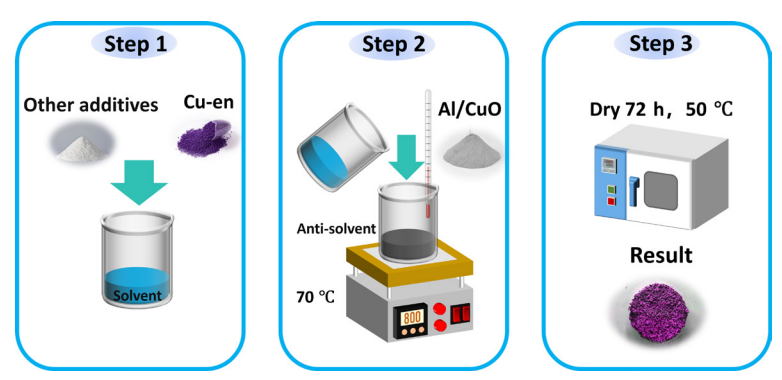


Figure 17. The preparation schematic illustration of solvent evaporation method

The preparation process of Al/CuO/Cu-en composites by spray drying method was presented in Figure 16. For a typical fabricating process, take 2-3% F_{2311} to dissolve in DMF, add 15% Cu-en and 1% PVP after it is completely dissolved, ultrasonic about 45 min. The solution turns purple and there is no solid phase, and it is loaded into the spray gun. Take aluminium powder and copper oxide powder and add ethyl acetate (or absolute ethanol) with constant stirring,

spray the liquid with a spray gun, stir for 5 h, and filter to obtain a composite solid powder.



Figure 18. The preparation schematic illustration of spray drying method

3.3 Characterization

The morphology of samples was characterized by a scanning electron microscope (SEM, Hitachi regulus 8100). Thermogravimetry-differential scanning calorimetry (TG-DSC, Netzsch STA 449F5) was used to evaluate the thermal properties of the samples, conducted from 50 to 500 °C with nitrogen atmosphere of 60 mL/min at the heating rate of 10 K/min. The combustion performances were investigated by open combustion behavior tests, and about 30 mg of sample was put onto an inverted cylindrical crucible and ignited with a nichrome wire (0.25 mm in diameter). The loaded wire was connected with a direct current power supply operated at 5.0 A. The combustion process was recorded by a high-speed camera (PHANTOM v 12.0 UX50) with a sampling rate of 2,000 frames per second to further estimate the ignition delay time and burning time.

3.4 Results and discussion

3.4.1 Thermal decomposition performance

The addition of Cu-en significantly improved the thermodynamic performance of the Al/CuO system, as shown in Figure 19. In the case where Cu-en was not added, the Al/CuO composite did not exhibit any exothermic peak. This lack of exothermic reaction could be attributed to the fact that the reaction might have occurred in a weak solid-state diffusion manner, without forming a large-scale exothermic combustion reaction.

By introducing Cu-en and using F_{2311} as a binder, three additional composite methods were applied, leading to three subsequent Differential Scanning Calorimetry (DSC) data sets. The analysis of these data sets is as follows.

The composite prepared by solvent evaporation, showed an exothermic peak at 260.75 °C. This exothermic peak corresponds to the heat released by the in-situ decomposition of Cu-en. However, no further exothermic peaks were observed with increasing temperature. This suggests that the degree of composite formation is not very high, meaning that Cu-en did not fully integrate into the Al/CuO system. As a result, the thermite reaction (Al and CuO) did not occur effectively, indicating incomplete incorporation of Cu-en into the system. The composite prepared by the spray drying method began to release heat at 383.04 °C and continued until 698.04 °C, with a total heat release of 1916.43 J. After the temperature reached 782.94 °C, another exothermic peak appeared. This dual peak phenomenon can be explained as follows: during the previous reaction, aluminium powder did not fully react, and the remaining aluminium started to melt at around 660 °C. This molten aluminium then continued to react with CuO, producing a second exothermic peak until 916.6 °C, releasing an additional 392.73 J of heat. Therefore, while the spray drying method increased the heat release of the Al/CuO system, it still exhibited incomplete reaction, as evidenced by the two exothermic peaks in the DSC data. This suggests that the composite prepared by spray drying was not homogeneous. The composite prepared by electrostatic spraying showed an exothermic peak at 353.13 °C, which continued until 804.62 °C. The total heat release was significantly higher, reaching 4702.05 J. Importantly, no second exothermic peak was observed, unlike the spray drying method. This suggests that the electrostatic spraying method led to a much more homogeneous composite, with Cu-en playing a significant catalytic role in the Al/CuO system, thereby ensuring a complete and efficient thermite reaction.

From the analysis of the DSC data, it is clear that the electrostatic spraying method resulted in the most uniform and efficient composite, leading to a significantly higher heat release and a single, sustained exothermic peak. The spray drying method, while improving heat release, still exhibited incomplete reactions and non-homogeneous mixing, as shown by the presence of two exothermic peaks. The solvent evaporation method, on the other hand, showed minimal reactivity and poor integration of Cu-en into the Al/CuO system, resulting in a lack of significant heat release.

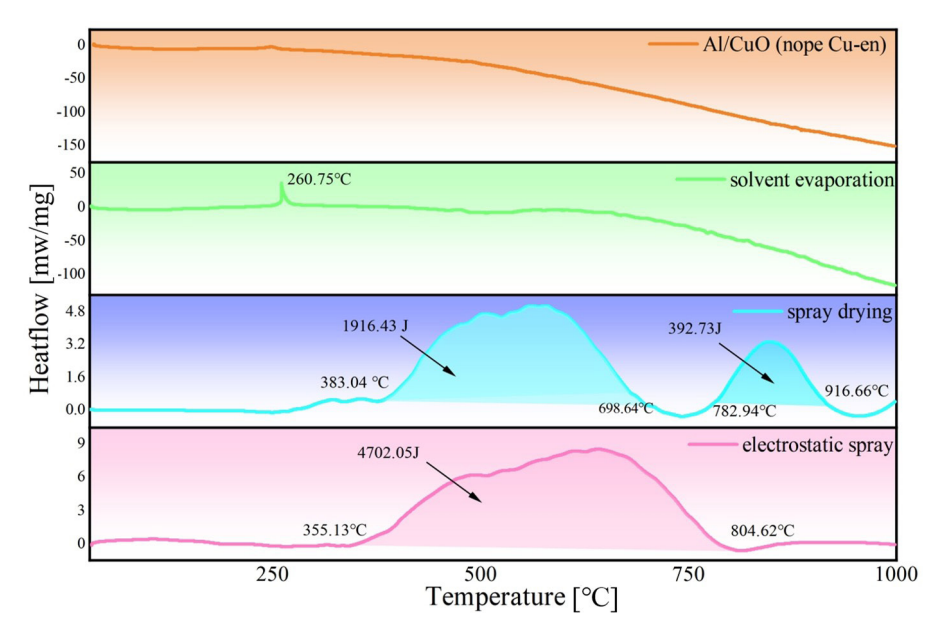


Figure 19. DSC test for each group at 10 K/min

According to the DSC results and a comprehensive analysis based on the properties of Cu-en, it is likely that Cu-en decomposes into more active copper ions or copper oxide at high temperatures. These substances can accelerate the oxidation reaction, which is why the electrostatic spraying group, which showed the best composite effect, has an earlier exothermic peak and increased heat release. The spray drying method, although somewhat less effective, still showed some improvement. In the solvent evaporation group, however, due to the uneven composite, local reactions may have occurred too quickly, leading to thermal instability or side reactions. Alternatively, Cu-en decomposition may produce other by-products (such as copper metal or complex oxides), which at high temperatures could influence the mass fractions of copper metal and aluminium oxide generated in the thermite reaction. As a result, no exothermic peak was observed in this group.

3.4.2 Combustion performance

Figure 20(a) shows the combustion images of the composite prepared by the solvent evaporation method. After the resistance wire was ignited, the flame began to form at 44 ms. By 59 ms, the combustion flame was clearly visible along with sparks. The flame displayed a blue-green color due to the decomposition

of Cu-en and the interaction with CuO in the system. From 144 to 180 ms, the flame continued to enlarge, and then, by 213 ms, it started to narrow, with sparks increasing. The flame extinguished at 354 ms. Figure 20(b) illustrates the combustion images of the spray drying group. In this group, the flame reached a high height almost immediately at 18 ms, and the combustion was more intense and brighter than that in Figure 20 from the solvent evaporation group. At 53 ms, a blue-green flame appeared, but its brightness had significantly decreased compared to 18 ms. The combustion continued until 296 ms, when the flame became progressively brighter and reached its maximum brightness. By 311 ms, the flame began to narrow. However, due to uneven mixing, the flame began to rise again and continued to grow until 646 ms, when it finally extinguished. The entire combustion duration was 646 ms, with the flame reaching its highest point at around 296 ms. The combustion was relatively more intense than in the solvent evaporation group, but the uneven mixing caused the flame to rise again, which corresponds with the DSC results shown in Figure 19. Figure 20(c) shows the combustion data for the electrostatic spraying group. This group exhibited a very quick ignition response with a small instant burst of combustion. The flame ignited almost instantly within 0.5 ms, and the brightness rapidly increased until reaching its peak at 8 ms. At 16 ms, the flame brightness began to decrease, and by 50 ms, the brightness had decreased to a level similar to that at 0 ms. However, the flame remained at a relatively high intensity. By 99 ms, the flame had essentially extinguished. The total combustion time was 99 ms, with an extremely fast ignition response and high combustion brightness, indicating that this group was well-mixed and generated a large amount of heat.

According to the analysis of the traces left on the platform after combustion, Figure 21 shows the combustion trace analysis for each method. Due to the rapid combustion, the composites prepared by Electrostatic Spraying left very deep combustion traces on the platform. The trace is overall red in color and forms a roughly circular shape with a diameter of about 4 cm, occupying approximately 4/5 of the platform. There were no visible unreacted particles remaining, indicating complete combustion in this area. The combustion trace of the composites prepared by spray drying was relatively smaller, concentrated mainly at the center, with a noticeable presence of unreacted particles. This suggests that the reaction did not occur uniformly, and some particles did not fully react during the combustion process. The combustion trace of the composites prepared by solvent evaporation was the smallest, with all the trace concentrated in the center, forming a circle with a diameter of about 1 cm. A small amount of reaction product residue was observed outside the circular area, indicating incomplete reaction and poor uniformity in the composite preparation.

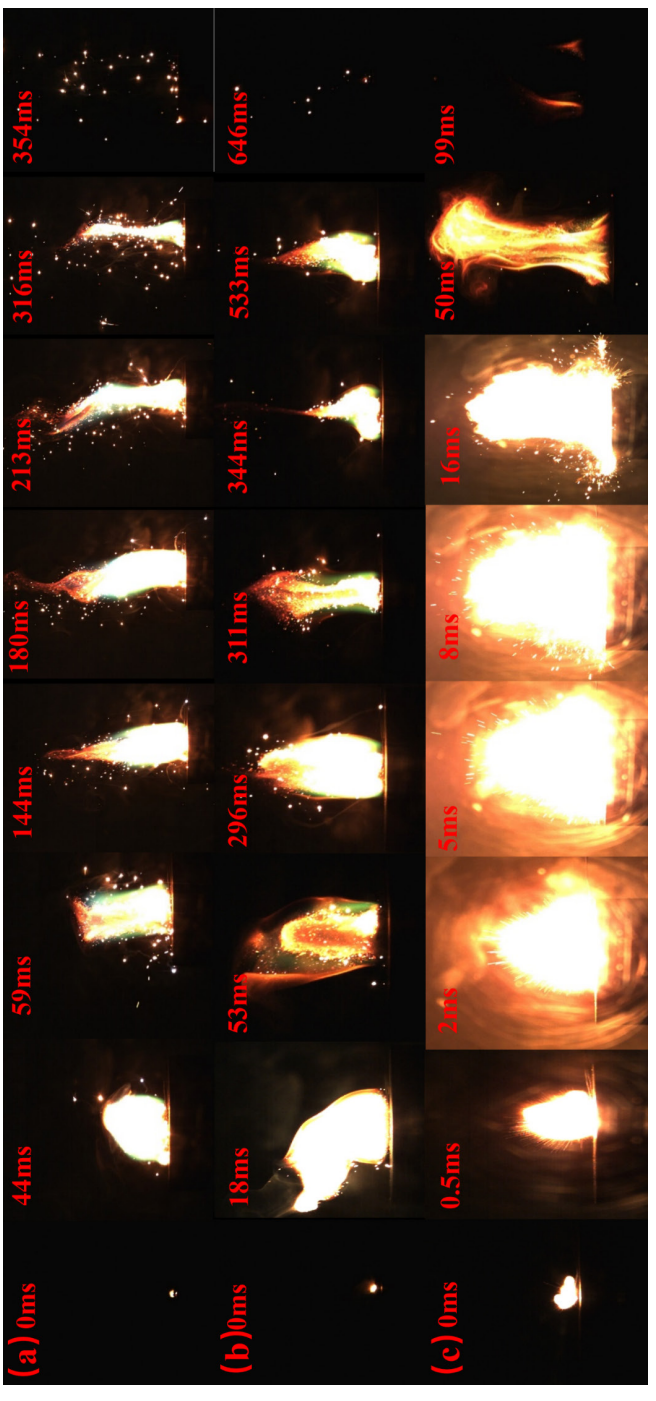


Figure 20. Combustion diagrams: solvent evaporation method (a), spray drying method (b) and electrostatic spraying method (c)

Copyright © 2025 Łukasiewicz Research Network – Institute of Industrial Organic Chemistry, Poland

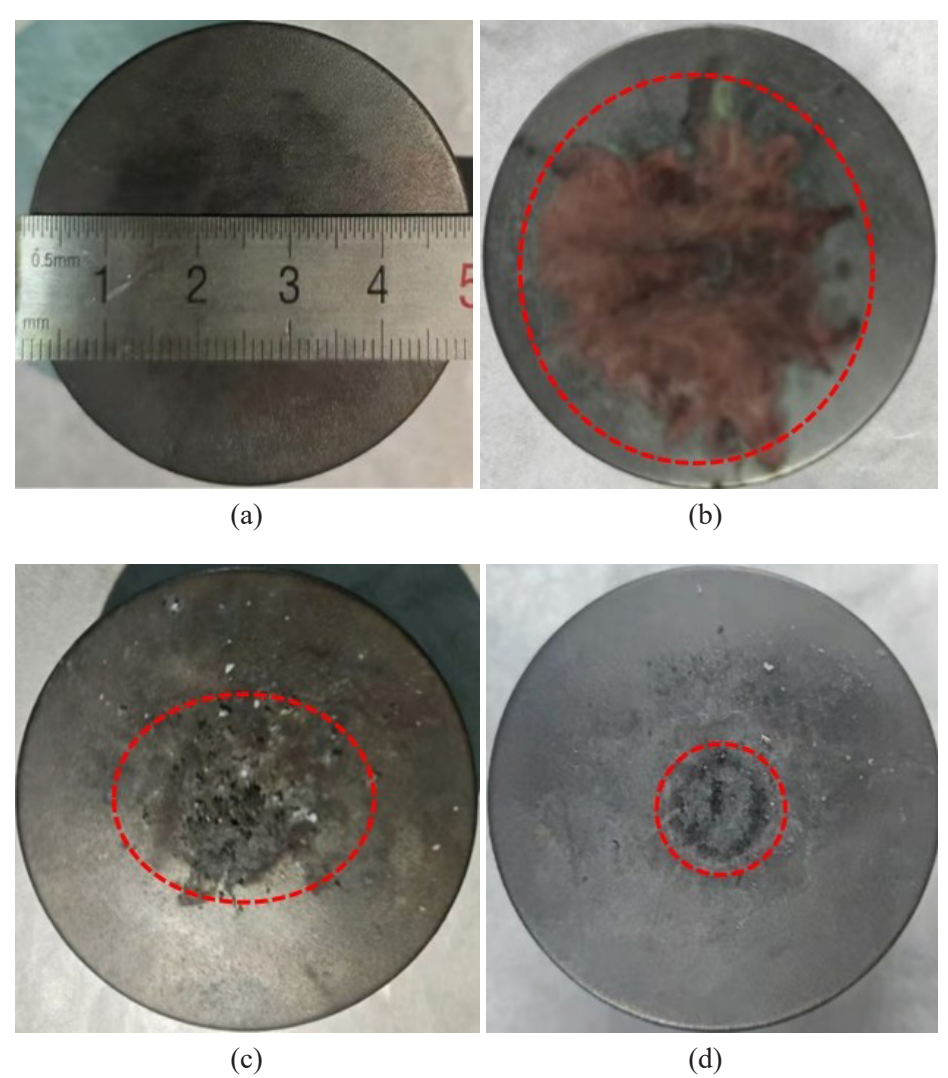
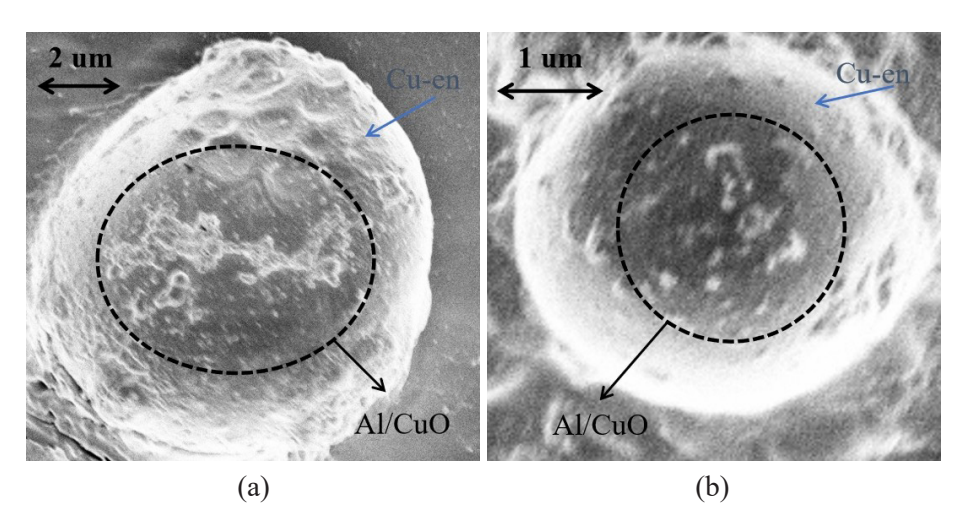


Figure 21. Post-combustion platform trace analysis: combustion test platform (a), electrostatic spraying (b), spray drying (c) and solvent evaporation (d)

3.4.3 Analysis of SEM

The morphological characteristics of the composites were observed using a scanning electron microscope (SEM). Since Cu-en was dissolved in DMF during the preparation process, it appeared mostly spherical under SEM observation and adhered to the surfaces of Al and CuO. Figure 22(a) shows the

SEM image of the composite prepared by spray drying. Upon closer examination, the composite exhibits a spherical-like morphology with an overall particle size of around 10 µm. Although Cu-en is distributed on the surface, it is mostly aggregated in one area, which is not conducive to full contact and reaction with Al/CuO during the combustion and decomposition of Cu-en. As a result, the outcomes in DSC and combustion tests did not achieve optimal performance. Figure 22(b) displays the composite prepared by electrostatic spraying, with an overall particle size of about 3-4 µm. The surface is smooth and forms complete spheres, with Cu-en relatively uniformly distributed on the surfaces of Al and CuO. This mode of attachment is more favorable for full contact among the components during the reaction. Cu-en directly burns and decomposes into nanometal oxides or nano-metals on the Al surface and acts directly within the system. Therefore, the composite prepared by electrostatic spraying performed better in DSC and combustion tests. Figure 22(c) illustrates the composite prepared by solvent evaporation. This group of composites appears as flattened spheres, with some parts of the surface edges beginning to form a spherical shape, but the majority remains non-spherical and uneven. A small amount of Cu-en adheres to the surfaces of Al and CuO. Combined with DSC and combustion test analyses. the poor thermodynamic performance of this group may be due to the irregular shape of Cu-en, leading to suboptimal catalytic performance after decomposition.



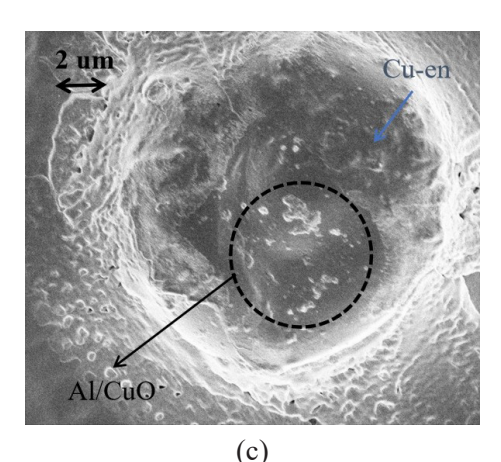


Figure 22. SEM images: spray drying (a), electrostatic spraying (b) and solvent evaporation (c)

4 Conclusions

- ♦ By setting up a 3×3 orthogonal experimental design, with flow rate, voltage, and receiving distance as the reference factors, and particle size, velocity, and residence time as the reference levels, the optimal process scheme was determined to be voltage 12 kV, receiving distance 25 cm, and flow rate 0.2 mL/min. The primary and secondary influencing factors were flow rate, voltage, and receiving distance. At the same time, based on the optimized process scheme, a control variable experiment was set up to summarize the influence patterns of flow rate, voltage, and receiving distance on particle size, etc. The relationship between the variables was expressed intuitively through fitting curves. It was found that the factor that had the greatest impact on particle size was flow rate, and as the flow rate increased, the particle size decreased continuously. This was described by a linear equation as y = −65092.86x + 12927.1.
- ♦ By introducing Cu-en into the Al/CuO system, the thermodynamic and combustion properties of the Al/CuO system were significantly improved. The compound prepared by electrostatic spray method had a peak temperature of exothermic reaction as early as 353.13 °C, with a heat release of up to 4702.05 J/g. Compared with the compound prepared by spray drying method, its heat release was approximately 2309.16 J/g higher. In the combustion test, the compound prepared by electrostatic spray method had the fastest

burning rate, with concentrated deflagration time and a wide range of burning rate. The SEM scanning electron microscope showed that the compound prepared by electrostatic spray method had the most regular shape and the smallest particle size. Based on the above analysis, through the electrostatic spray method, Cu-en was perfectly integrated into the Al/CuO system, which greatly catalyzed the progress of the aluminum thermal reaction.

Acknowledgement

This work was supported by the National Natural Science Foundation of China (No. 22275150).

References

- [1] Dwivedi, B.; Bhardwaj, D.; Choudhary, D. Biowaste-Mediated Synthesis of CeO₂-TiO₂ Nanoparticles: An Efficient Recoverable Nanocatalyst for the Solvent-Free Synthesis of Antipyrine Derivatives and Their Biological Evaluation. *ChemistrySelect* **2024**, *9*(43) paper e202403884; https://doi.org/10.1002/slct.202403884.
- [2] Md Radzi, M.R.; Rosli, S.N.A.; Yusoff, M.H.M.; Zainal, S. Production of 1,3-Propanediol *via In Situ* Glycerol Hydrogenolysis in Aqueous Phase Reforming using Bimetallic W-Ni/CeO₂. *Environ. Sci. Pollut. Res. Int.* **2024**, *32*: 19372-19389; https://doi.org/10.1007/s11356-024-35262-x.
- [3] Trembach, B.; Silchenko, Y.; Balenko, O.; Hlavchev, D.; Kulahin, K.; Heiko, H.; Bellorin-Herrera, O.; Khabosha, S.; Zakovorotnyi, O.; Trembach I. Study of the Hardfacing Process Using Self-shielding Flux-cored Wire with an Exothermic Addition with a Combined Oxidizer of the Al-(CuO/Fe₂O₃) System. *Int. J. Adv. Manuf. Technol.* **2024**, *134*: 3985; https://doi.org/10.1007/s00170-024-14324-x.
- [4] Lewetegn, K.; Birhanu, H.; Liu, Y.; Taddesse, P. Synthesis of Zn_{0.87}(Fe, Al)_{0.065}O-MO (MO = NiO, Fe₂O₃, CuO, and CoO) Nanocomposites: Structural, Vibrational, Optical and Antibacterial Studies. *J. Mol. Struct.* 2025, 1319 paper 139401; https://doi.org/10.1016/j.molstruc.2024.139401.
- [5] Abdelaziz, S.M.; Fakher, W.; Nada, R.H.; Ismail, A.M. Effect of CuO Nanostructure Addition and Cooling Rate on the Microstructure and Mechanical Characteristics of Hypoeutectic Al-2wt.%Si Alloy. *J. Mater. Eng. Perform.* 2024, 34: 9476-9492; https://doi.org/10.1007/s11665-024-09821-9.
- [6] Ejaz, Y.; Alrowaily, A.W.; Alyousef, H.A.; Alotaibi, B.M.; Dahshan, A.; Alahmari, S.D.; Karim, Md R. CuO/CeAlO₃ Nanocomposite with Enhanced Electrocapacitive Performance for Supercapacitor Applications. *Ceram. Int.* 2024, 50: 30628-30636; https://doi.org/10.1016/j.ceramint.2024.05.361.

- [7] Liu, Z.; He, C.; Zhuang, Z.; Li, S.; Feng, X.; Liu, J. Ignition and Energy Release Performance of Dual-Oxidant Al/MnO₂/CuO Ternary Thermites under Rapid Heating Conditions. *Propellants Explos. Pyrotech.* **2024**, *49*(7) paper e202400005; https://doi.org/10.1002/prep.202400005.
- [8] Xiong, K.; Wang, Z.; Liu, R.; Nie, H.; Yan, Q.L. Probing on Mutual Interaction Mechanisms of the Ingredients of Al/CuO/PVDF Nanocomposites. *Langmuir* **2023**, 39: 13850-13862; https://doi.org/10.1021/acs.langmuir.3c01299.
- [9] Zhou, Y.; Wang, Y.; Zhang, Z.; Li, F.; Cheng, J.; Ye, Y.; Xu, J.; Shen, R. Low Air Pressure Self-Sustaining Combustion Performances of 3D Direct Writing Al/CuO Film. *Chem. Eng. J.* **2023**, *473* paper 145031; https://doi.org/10.1016/j.cej.2023.145031.
- [10] Ao, W.; Wen, Z.; Liu, L.; Wang, Y.; Zhang, U.; Liu, P.; Qin, Z.; Li, L.K.B. Combustion and Agglomeration Characteristics of Aluminized Propellants Containing Al/CuO/PVDF Metastable Intermolecular Composites: A Highly Adjustable Functional Catalyst. *Combust. Flame* 2022, 241 paper 112110; https://doi.org/10.1016/j.combustflame.2022.112110.
- [11] Zhu, Y.; Zhou, X.; Xu, J.; Ma, X.; Ye, Y.; Yang, G.; Zhang, K. *In Situ* Preparation of Explosive Embedded CuO/Al/CL20 Nanoenergetic Composite with Enhanced Reactivity. *Chem. Eng. J.* **2018**, *354*: 885-895; https://doi.org/10.1016/j.cej.2018.08.063.
- [12] Yin, Y.; Li, X.; Shu, Y.; Guo, X.; Bao, H.; Li, W.; Zhu, Y.; Li, Y.; Huang, X. Fabrication of Electrophoretically Deposited, Self-Assembled Three-Dimensional Porous Al/CuO Nanothermite Films for Highly Enhanced Energy Output. *Mater. Chem. Phys.* **2017**, *194*: 182-187; https://doi.org/10.1016/j.matchemphys.2017.03.018.
- [13] Wang, D.; Dong, C.; Yi, Z.; Qi, X.; Li, Y.; Zhang, L.; Zhu, C. Preparation of Activated Carbon Nanostructured Al@CuO with Low Static Sensitivity and High Reactivity. *ACS Omega* **2024**, *9*(14): 15854-15860; https://doi.org/10.1021/acsomega.3c08086.
- [14] He, M.; Xie, Y.; Ni, J.; Jian, Y.; Song, S.; Bao, H.; Zeng, X.; Li, X.; Wang, Q. Electrophoretic Deposition of Al/CuO Energetic Materials and Their Heat Release Performance. *Int. J. Electrochem. Sci.* 2020, 15(12): 12015-12029; https://doi.org/10.20964/2020.12.23.
- [15] Lv, X.; Gao, Y.; Cui, Y.; Wang, C.; Zhang, G.; Wang, F.; Liu, P.; Ao, W. Study of Ignition and Combustion Characteristics of Kerosene-based Nanofluid Fuel Containing *n*-Al/CuO Thermite. *Fuel* **2023**, *331* paper 125778; https://doi.org/10.1016/j.fuel.2022.125778.
- [16] Lou, M.; Zhang, Y.; Zhang, Y.; Xie, H.; Qiu, B.; Wang, J. Additive Exploration of Al/CuO Aluminium Thermite Systems. *Innovation Dev.* **2024**, *8*: 1-8; https://doi.org/10.54097/wckx5x79.
- [17] Song, N.; Yang, L.; Han, J.; Liu, J.C.; Zhang, G.Y.; Gao, H.X. Catalytic Study on Thermal Decomposition of Cu-en/(AP, CL-20, RDX and HMX) Composite Microspheres Prepared by Spray Drying. New J. Chem. 2018, 42: 19062-19069; https://doi.org/10.1039/C8NJ04166K.

- [18] Chen, F.; Deng, X. Droplet Breakup in Electrostatic Spray based on Multiple Physical Fields. *Adv. Powder Technol.* **2022**, *33*(12) paper 103842; https://doi.org/10.1016/j.apt.2022.103842.
- [19] Lin, P.; Chen, Q.; Liu, Y.; Hu, X.; Zhu, Z. Prediction of Newtonian Droplet Breaking Time from a Capillary at Low Weber Numbers. *ACS Omega* **2022**, *7*(27): 23890-23898; https://doi.org/10.1021/acsomega.2c02602.
- [20] Lu, L.; Pei, Y.; Qin, J.; Peng, Z.; Zhong, K. Analysis of the Breaking Process and the Components of the Crown Structure after a Single Droplet Hits Thin Liquid Film. *Appl. Therm. Eng.* **2023**, *219* paper 119514; https://doi.org/10.1016/j. applthermaleng.2022.119514.
- [21] Tüfekci, M.; Dear, J.; Salles, L. A finite element based approach for nonlocal stress analysis for multi-phase materials and composites. *Eng. Comput.* **2024**, *41*(2): 1-19; https://doi.org/10.1007/s00366-024-02076-x.
- [22] Li, Y.; Guo, H.; Ma, X.; Wang, J.; Xu, H. Droplet Dynamics of DI Spray from Sub-Atmospheric to Elevated Ambient Pressure. *Fuel* **2016**, *179*: 25-35; https://doi.org/10.1016/j.fuel.2016.03.047.
- [23] Osman, H.; Castle, G.S.P.; Adamiak, K. Numerical Study of Particle Deposition in Electrostatic Painting Near a Protrusion or Indentation on a Planar Surface. *J. Electrostat.* **2015**, 77: 58-68; https://doi.org/10.1016/j.elstat.2015.07.005.
- [24] Bisquert, L.; Ruiz-Gutiérrez, É.; Pradas, M.; Ledesma-Aguilar, R. Competing Bifurcations Determine Symmetry Breaking during Droplet Snaps on Smooth Patterned Surfaces. *Langmuir* **2024**, *40*(46): 24387-24396; https://doi.org/10.1021/acs.langmuir.4c02908.
- [25] Grifoll, J.; Rosell-Llompart, J. Continuous Droplets' Charge Method for the Lagrangian Simulation of Electrostatic Sprays. *J. Electrostat.* **2014**, *72*: 357-364; https://doi.org/10.1016/j.elstat.2014.06.011.

Authorship contribution statement

Wei Ji: conception, methods

Yilong Duan: methods, performing the experimental part

Lei Liu: performing the statistical analysis Lingxin Wang: other contribution to the publication

Wei Ji and Yilong Duan contributed equally to this work and are co-first authors.

Submitted: May 06, 2025 Revised: September 25, 2025

First published online: September 30, 2025